Spatial density maps from a debris cloud

Liam Healy
Naval Research Laboratory, Washington, DC
Scott Kindl
Naval Research Laboratory, Washington, DC
Christopher Binz
Naval Research Laboratory, Washington, DC

Abstract

A debris cloud from a fragmentation on orbit may be modeled by transformation of variables from the instantaneous velocity distribution at the fragmentation time to the spatial distribution at some elapsed time later. There are no Gaussian distributions assumed and the evolution map is quite nonlinear, being derived from the solution of the Lambert, two-point boundary value, problem and the state transition matrix for unperturbed propagation, so the traditional tools of analysis that assume these qualities fail dramatically. The transformation of variables technique does not suffer from any such assumptions, and unlike the Monte Carlo method, is not subject to sampling errors or approximations.

Structures and features are evident in the density maps, and these structures show promise for simplified approximation of the density map. Most prominent of the structures is the well-known pinch point at the fragmentation location in inertial space. The anti-pinch line, or wedge, is also observed. Bands on the opposite side of the fragmentation are very noticeable, and their existence may be motivated from simple orbit dynamics. These bands make the anti-pinch line actually more of a set of anti-pinch line segments.

By computing these density maps over time, the evolution may be studied. There is a density generator, a density band at roughly the same altitude as the pinch point, that cycles around the earth and appears a source of the bands, with newly created bands moving radially outward and diminishing in density. Although the initial velocity distribution affects the final spatial distribution, the Lambert solutions, which are the most time consuming to compute, need only be computed once. Therefore, different initial distributions may be changed and the results recomputed with relative speed. A comparison of the effects of initial distributions is shown in this paper.

1 Introduction

When an instantaneous fragmentation happens on orbit, a single object suddenly becomes multiple objects, and the orbits of each of these pieces will be different from the original, *source* orbit. In fact, the fragmentation adds a random impulsive delta-v to each piece, and analysis may proceed as would a maneuver of such a type. Because this delta-v has in general no constraints, except perhaps a limit to its magnitude, the trajectory of such pieces can be almost anywhere physically possible.

For decades, researchers have employed various techniques to study the evolution of the "cloud" of fragments. Jehn [1] divided the post-fragmentation time interval into four phases, labeled "A," "B," "C," and "D." In phase A, the cloud of fragments is a pulsating ellipsoid, being still confined relatively close to the source orbit. The pulsation is seen to occur every orbital period; the extent of

the cloud decreases and hence its density increases as it returns to the fragmentation point. In phase B, the shape of the cloud is a torus with a pinch point and pinch line. This may occur as soon as a few hours after fragmentation; what drives the spreading of fragments into the toroidal ring matching the source orbit is a velocity change component in the in-track direction that changes the orbital periods of the fragments. In phase C, perturbations, notably the J_2 geopotential perturbation, cause the nodal regression which smears out the torus into a spherical shell truncated at the polar caps. Finally in phase D, if the orbit is low enough, the evenly distributed band loses population to atmospheric drag lowering and ultimately deorbiting the fragments. In this study, we focus on phases A and B.

Hujsak [2], almost simultaneously with Jehn, derived a nonlinear dynamical model of the relative motion for the purpose of analysis of debris density from breakup through what Jehn would call phase B. By including select nonlinear terms and using a generalization of the Hill-Clohessy-Wiltshire equations for elliptical orbits, he was able to derive equations useful even far from the source orbit. He shows the inverse of the relative motion transformation is an approximate solution for the whole orbit Lambert (boundary value) problem. Including the geopotential J_2 perturbation, he is able to analyze debris density differentially as function of breakup velocity distribution. He found that particle density can vary by four orders of magnitude, and attributes increases in density away from the pinch point to perturbations. While we find the relative motion approach too limiting and therefore take a different approach, we regard Hujsak's study as a novel and pioneering idea for debris cloud evolution studies, and in a very significant sense inspired our present undertaking. His claim of four orders of magnitude is plausible, but concentrations of density occur even in an unperturbed model.

Often, these analyses proceed with explicit or implicit assumptions of the initial velocity distribution. Sometimes, for example, isotropic, or uniform in all directions, sometimes uniformly distributed in magnitude within some bound. The analysis may be based on some established fragmentation model, such as the NASA model [3], but more often it is not. There is much that can be concluded without a specific creation model, but having such a model allows one to investigate in greater depth the collective behavior of the fragments.

The purpose of this study is to determine the distribution in space of the fragments within a few tens of source orbits, to determine where areas of concentrated density are and whether they are static or change dramatically over this time period. In order to do this, we develop the mathematical tools needed. In this regard, we have taken a fresh approach. In order to find the distribution in space at the end of the time interval from the distribution in velocity at the beginning, we use the transformation of variables technique. This then provides a set of data which can be used to apply to any velocity distribution to determine the spatial distribution. The spatial distribution we seek is a function giving the *normalized number density* at any point in space, and it is measured in units of reciprocal volume, such as km^{-3}. Equally, this can be considered a probability density function; for example, the probability of finding a single vehicle in a location after a maneuver of uncertain delta-v.

The transformation of variables method tells us how to compute a density after mapping the domain space through a transformation. It needs two pieces of information: the inverse image points under the initial velocity to final position mapping, and the determinant of the Jacobian of the map at each of those points. Once those have been computed for a point in the domain space of the transformation (velocities), the data may be saved as a distribution map, and the computation of a later spatial distribution from an initial velocity distribution may be performed as a value look-up, multiplication and addition, a relatively fast calculation.

In orbital terms, the initial velocity to final position mapping is, because the initial position is assumed fixed, simply the initial value problem for orbit dynamics. Here, unperturbed two-body

(Kepler) motion is assumed, and the propagator used are the Lagrange coefficients f and g. The inverse map needed is the two-point boundary value problem, i.e., the Lambert problem. From every point $\boldsymbol{r}_2$ at the end of the time interval and from the fixed initial location of the fragmentation $\boldsymbol{r}_1$, the task is to find the initial velocities $\dot{\boldsymbol{r}}_1$ that solve the two-body motion. Then, for each of those initial values, to find the determinant of the Jacobian of the orbit propagation problem.

Astrodynamics, and before it, celestial mechanics, has been focused on *point dynamics*, that is, how a single satellite (or planet) moves about a single attracting body. For unperturbed motion particularly, this problem is well in hand; not just the initial value problem of orbit propagation, but the boundary value, or Lambert, problem is as well. What we propose here is new: that point dynamics induces a *cloud dynamics*, an evolution of a density distribution over time. This is significantly more difficult to compute than the point dynamics case, but the rewards are potentially very large.

2 An orbital density map

An *orbital density map* as we define it is the density of orbiting objects in Cartesian space around the earth. This density is a function of the position, and of time. It may be a distribution of actual objects, such as fragments, but it may also be a probability distribution, which can be considered the distribution of virtual objects. A probability density or normalized number density function will integrate to one over the whole volume; a general density function will not have a specified integral, and might integrate to the total number of pieces, for example.

In order to find the density map, we will need to know the location of the fragmentation $\boldsymbol{r}_1$ and the distribution of velocities. The distribution of locations $\boldsymbol{r}_2(t)$ for an elapsed time t can be computed from orbit mechanics using the *transformation of variables* technique for density functions. The transformation (or change) of variables technique [4] can be stated simply. Given a function F from a space X to a space Y, a density function G_X in the space X can be transformed into one in the space Y by summing over all the points in the inverse image $F^{-1}(y)$ ($y \in Y$) divided by the absolute value of the determinant of the Jacobian matrix of F

$$G_Y(y) = \sum_{x \in F^{-1}(y)} \frac{G_X(x)}{|\det J_F(x)|}, \tag{1}$$

where x and y can be vectors. The Jacobian matrix J_F is the matrix of partial derivatives of the function F. When the inverse image is a continuum rather than a discrete set of points, the sum must be replaced with an integral.

In the present application, the space X is three dimensional, the velocity at the fragmentation point, and the space Y, also three dimensional, is the location of the fragment at a fixed later time. We seek the orbital density function G_Y given the velocity distribution G_X. For each value of the elapsed time after the fragmentation, the function G_Y must be computed for all points. However, once computed and stored, the values x in the inverse image of each point y, and the corresponding Jacobian determinant $|\det J_f(x)|$ may merely be looked up in a velocity distribution function G_X from which G_Y can be rapidly calculated.

There are clearly two pieces to the problem: finding the inverse images $F^{-1}(y)$ and computing the forward Jacobian determinant. In the orbital context, the forward function F is the initial value problem for orbit mechanics; given an initial position $\boldsymbol{r}_1$ and velocity $\dot{\boldsymbol{r}}_1$, find the position after time t, $\boldsymbol{r}_2$ and $\dot{\boldsymbol{r}}_2$. The inverse image calculation amounts to the two-point boundary value, or Lambert, problem. These are covered in order in the next two sections.

3 The initial value problem

Unperturbed orbits may be propagated using the Lagrange f and g coefficients. Because an orbit lies in a plane, any point on the orbit and any velocity vector can be described by two vectors that span the plane. Because they cannot be colinear, the initial position $\boldsymbol{r}_1$ and velocity $\dot{\boldsymbol{r}}_1$ may serve as those basis vectors, with suitable coefficients:

$$\boldsymbol{r}_2 = f(t)\boldsymbol{r}_1 + g(t)\dot{\boldsymbol{r}}_1 \tag{2a}$$

$$\dot{\boldsymbol{r}}_2 = \dot{f}(t)\boldsymbol{r}_1 + \dot{g}(t)\dot{\boldsymbol{r}}_1. \tag{2b}$$

The initial conditions are must match these values when $t = 0$,

$$f(0) = 1, \quad \dot{f}(0) = 0 \tag{3a}$$

$$g(0) = 0, \quad \dot{g}(0) = 1. \tag{3b}$$

These form a set of vector differential equations which can be solved for the coefficients f and g. Although they are time dependent, we will drop the function arguments henceforth. However, it is important to remember that these "coefficients" are actually functions of $\boldsymbol{r}_1$ and $\dot{\boldsymbol{r}}_1$, because we will need to take the partial derivatives for the Jacobian.

There are different forms for the Lagrange coefficients; we use the eccentric anomaly formulation [5],

$$f = 1 - \frac{a}{r_1}(1 - \cos\Delta E) \tag{4a}$$

$$g = t - \sqrt{\frac{a^3}{\mu}}(\Delta E - \sin\Delta E) \tag{4b}$$

$$\dot{f} = \frac{-\sqrt{\mu a}\sin\Delta E}{r_2 r_1} \tag{4c}$$

$$\dot{g} = 1 - \frac{a}{r_2}(1 - \cos\Delta E), \tag{4d}$$

where a is the semimajor axis, $\Delta E = E_2 - E_1$ is the change in eccentric anomaly between the two points, and μ is the gravitational constant. In order to use these coefficients, the semimajor axis and change in eccentric anomaly must be computed from $\boldsymbol{r}_1$ and $\boldsymbol{r}_2$, and the latter requires the application of Kepler's equation among other things. Typically in this application a Newton method is used to solve Kepler's equation at each point. It is important to note that E_2 must be greater than E_1, and it must include whole orbits, that is to say, each whole orbit adds another 2π to the change. No angle normalization (reduction to a range $-\pi$ to π or 0 to 2π) for E_2 is permitted here.

The Jacobian matrix needed for the transformation of variables in this problem is 3×3

$$J = \frac{\partial \boldsymbol{r}_2}{\partial \dot{\boldsymbol{r}}_1} = \begin{bmatrix} \frac{\partial r_{2I}}{\partial v_{1I}} & \frac{\partial r_{2I}}{\partial v_{1J}} & \frac{\partial r_{2I}}{\partial v_{1K}} \\ \frac{\partial r_{2J}}{\partial v_{1I}} & \frac{\partial r_{2J}}{\partial v_{1J}} & \frac{\partial r_{2J}}{\partial v_{1K}} \\ \frac{\partial r_{2K}}{\partial v_{1I}} & \frac{\partial r_{2K}}{\partial v_{1J}} & \frac{\partial r_{2K}}{\partial v_{1K}} \end{bmatrix}, \tag{5}$$

where derivatives of each of the three Cartesian components I, J, K are shown. This matrix is one 3×3 block of the 6×6 state transition matrix for orbit dynamics. It was computed by Battin [6],

and Battin's presentation was untangled by Arora et al. [7]. Equations (38)–(44), (47), and (50) of the latter publication form a clear algorithm from inputs $\boldsymbol{r}_1$, $\boldsymbol{r}_2$, Δt and f (eq. (4a)), g (eq. (4b)), $\dot{f}$ (eq. (4c)), $\dot{g}$ (eq. (4d)) and the semimajor axis a; the latter set come out of the Lambert solver (section 4). The formulas are

$$U_1 = -\frac{r_1 r_2 \dot{f}}{\sqrt{\mu}} \tag{6a}$$

$$U_2 = r_1(1-f) \tag{6b}$$

$$U_3 = \sqrt{\mu}(t-g) \tag{6c}$$

$$U_4 = U_1 U_3 - \frac{1}{2}(U_2^2 - U_3^2/a) \tag{6d}$$

$$\sigma_1 = \frac{\boldsymbol{r}_1 \cdot \dot{\boldsymbol{r}}_1}{\sqrt{\mu}} \tag{6e}$$

$$\sigma_2 = \frac{\boldsymbol{r}_2 \cdot \dot{\boldsymbol{r}}_2}{\sqrt{\mu}} \tag{6f}$$

$$\chi = \frac{t\sqrt{\mu}}{a} + \sigma_2 - \sigma_1 \tag{6g}$$

$$U_5 = a\left(\frac{1}{6}\chi^3 - U_3\right) \tag{6h}$$

$$\bar{C} = \frac{1}{\sqrt{\mu}}\left(3U_5 - \chi U_4 - \sqrt{\mu} U_2 t\right) \tag{6i}$$

$$\frac{\partial \boldsymbol{r}_2}{\partial \dot{\boldsymbol{r}}_1} = \frac{r_1}{\mu}(1-f)\left[(\boldsymbol{r}_2 - \boldsymbol{r}_1) \otimes \dot{\boldsymbol{r}}_1 - (\dot{\boldsymbol{r}}_2 - \dot{\boldsymbol{r}}_1) \otimes \boldsymbol{r}_1\right] + \frac{\bar{C}}{\mu}\dot{\boldsymbol{r}}_2 \otimes \dot{\boldsymbol{r}}_1 + gI, \tag{6j}$$

where I is the 3×3 identity matrix and "$\otimes$" represents the outer product, forming a 3×3 matrix from two 3-vectors.

4 The boundary value problem

4.1 All solutions

The inverse image needed for the transformation of variables is a matter of finding the correct initial velocity $\dot{\boldsymbol{r}}_1$ such that together with the known fragmentation location $\boldsymbol{r}_1$, and the elapsed time t, the correct final location $\boldsymbol{r}_2$ is obtained. That is, t, $\boldsymbol{r}_1$ and $\boldsymbol{r}_2$ are given, and $\dot{\boldsymbol{r}}_1$ must be found. This is the classic Lambert problem, or two-point boundary value problem for orbit mechanics. Over the centuries since it was first posed, numerous methods have been developed for solving this problem. Some methods do better on or are only applicable for certain kinds of orbits, for example, short arcs, bound orbits, or those that go less than a whole orbit; for this application, we cannot restrict the kinds of orbits.

Between any two position vectors, an orbit can go in one of two directions. If the transfer angle is less than 180 degrees (or between 360 and 540 degrees, etc.), the arc is considered *short* way, if between 180 and 360 degrees, it is considered *long* way. Note the terms refer to the angle; the amount of time is the same in both cases, as assumed in the problem. If the earth center and the two points are colinear, there is no unique solution because the plane is undetermined, but the planar elements a, e and true anomaly can be determined.

If the trajectory passes the initial point $\boldsymbol{r}_1$ at least once before t has elapsed, the trajectory is a *whole orbit* trajectory (customarily called "multi-revolution"); it will pass $\boldsymbol{r}_1$ $N \geq 1$ times before

the elapsed time is up. If it does not pass $\boldsymbol{r}_1$ before the elapsed time is up, it is a *zero orbit* case, or $N = 0$. All possible cases of non-negative integer N need to be examined in the Lambert algorithm.

A zero orbit trajectory can be of any conic section, but a whole orbit must be a bound orbit, i.e., circular or elliptical. While there is a solution for a zero orbit trajectory for any pair of points and time, assuming unlimited speed is possible, the whole orbit case has a minimum time. As N increases, this minimum time increases. Therefore, the search for solution is finite; if N is high enough that there are no solutions because the elapsed time is less than the minimum time, then no higher value of N need be searched.

Our application is unique among typical uses of Lambert solvers: we must obtain all solutions for a given set of boundary conditions and time; that is, all inverse images are necessary to form the sum in eq. (1). This includes all conic sections circular, elliptical, parabolic, and hyperbolic, both directions, and all possible revolution counts N.

The preceding exposition refers to the mathematical solution of the Lambert problem. Not all mathematical solutions are physical solutions; if the geocentric distance becomes less than the radius of the earth over the trajectory, it is not physically possible. Therefore, after determining a solution mathematically, it must be checked for minimum geocentric distance. If it is a whole orbit trajectory, that is the perigee radius. If it is zero orbit, and the trajectory crosses perigee, then again the perigee radius is the minimum geocentric distance. If the trajectory doesn't cross perigee, then the minimum geocentric distance is given by the smaller of the distances at the endpoints r_1 or r_2.

Another possible physical limitation is the velocity. If the escape velocity is not a possibility because, for instance, the energy of the fragmentation is known to be too low, then the unbound (parabolic and hyperbolic) orbits need not be considered. A velocity limit means that after a certain amount of time, there is a lower limit on N above zero, because the orbit needs a high enough orbital period to have that low an N. For example, if $\boldsymbol{r}_1$ and $\boldsymbol{r}_2$ are antipodal, then after one day, $N = 1$ is only possible if there is enough velocity to reach a 16 hour orbit from the fragmentation location.

Regardless of the Lambert algorithm used, a solver is always necessary, because all algorithms involve some sort of root solving of a function that is not invertible analytically. The solver is typically a standard algorithm such as a Newton method (if a derivative is available), or a bisection solver.

4.2 Lambert algorithm

Battin's hypergeometric [6] method gives consistently complete sets of solutions for all types of orbits. The core Lambert algorithm computes a and ΔE; the Lagrange coefficients are then used to solve for the initial velocity using eq. (2a). The Lambert theorem states that the elapsed time Δt is a function only of semimajor axis (an unknown in the Lambert problem), the sum of the geocentric distances $r_1 + r_2$, the chord length $c = |\boldsymbol{r}_2 - \boldsymbol{r}_1|$, whether the object went the long way (past the antipodal line) or the short way, and how many times N it passed the initial position $\boldsymbol{r}_1$ before the elapsed time. The Battin method computes a "normalized time," the time times the mean motion of the minimum energy orbit (see (7.32) in [6])

$$\sqrt{\frac{\mu}{a_{\mathrm{m}}^3}}\Delta t = \frac{2\pi N}{(1-x^2)^{3/2}} + \frac{4}{3}\eta^3\ {}_2F_1\left(3, 1; \frac{5}{2}; S_1\right) + 4\lambda\eta, \tag{7}$$

where N is the whole orbit count. Other quantities needed are computed in succession

$$s = \frac{r_1 + r_2 + c}{2} \tag{8}$$

$$a_{\mathrm{m}} = \frac{s}{2} \tag{9}$$

$$\lambda = \pm\sqrt{1 - \frac{c}{s}} \tag{10}$$

$$y = \sqrt{1 - \lambda^2(1 - x^2)} \tag{11}$$

$$\eta = y - \lambda x \tag{12}$$

$$S_1 = \frac{1}{2}(1 - \lambda - x\eta); \tag{13}$$

a_{m} is the minimal semimajor axis. The sign for λ is chosen on the short way/long way information; if the short way, the positive sign is taken, if the long way, the negative. The variable $x > -1$ is the unknown that must be solved. The function ${}_2F_1$ is a hypergeometric function. The gravitation constant is given by μ.

The variable x must be found that satisfies (7Lambert algorithmequation.0.7). Many root-solving techniques can make use of the derivative of the right hand side. The derivative of the hypergeometric function is another hypergeometric function[1], so the derivative of the right hand side of eq. (7) is

$$\frac{6\pi N x}{(1 - x^2)^{5/2}} - \frac{4}{5}(px + \eta)\eta^3\, {}_2F_1\left(4, 2; \frac{7}{2}; S_1\right) + 4\lambda p + 4p\eta^2 {}_2F_1\left(3, 1; \frac{5}{2}; S_1\right) \tag{14}$$

with

$$p = \frac{x\lambda^2}{y} - \lambda. \tag{15}$$

For the zero orbit case, presuming there is enough velocity, there is no minimum time to get to another point (except the time it takes light to travel between the points), so all solutions must be found. On the other hand, for the whole orbit case $N \geq 1$, there is a minimum time $t_{\min}(N)$ such that if $\Delta t < t_{\min}(N)$, no solution exists. For each additional whole orbit, this minimum time increases $t_{\min}(N + 1) > t_{\min}(N)$, so if it is found for a particular N that the minimum time is too high, the search with increasing N may be terminated for the input conditions. This leads to the concept of the maximum orbit count, a function of the desired elapsed time, $N_{\max}(\Delta t)$, beyond which no solutions are to be found.

Figure 1 shows a curve of normalized time versus x by whole orbit N for

$$\boldsymbol{r}_1 = \begin{bmatrix} 7278.1363 \\ 0.0 \\ 0.0 \end{bmatrix} \text{km}, \quad \boldsymbol{r}_2 = \begin{bmatrix} -10000.0 \\ 3750.0 \\ 0.0 \end{bmatrix} \text{km}. \tag{16}$$

For this case, each normalized time unit represents 1332.05s, so 24 hours is 64.862 normalized time units, represented by the dashed line in the figure. The plot shows only short way curves; it is clear that $N = 0$ has one such solution and each of $N = 1, \ldots, 9$ has two solutions. The minimum time for $N \geq 10$ is too large for there to be any solutions for 24 hours. The plot of long way curves looks similar and doubles the number of solutions. The Battin variable is greater than or equal to one $x \geq 1$ for unbound orbits, which is only possible if $N = 0$.

[1] `http://functions.wolfram.com/HypergeometricFunctions/Hypergeometric2F1/20/01/05/`

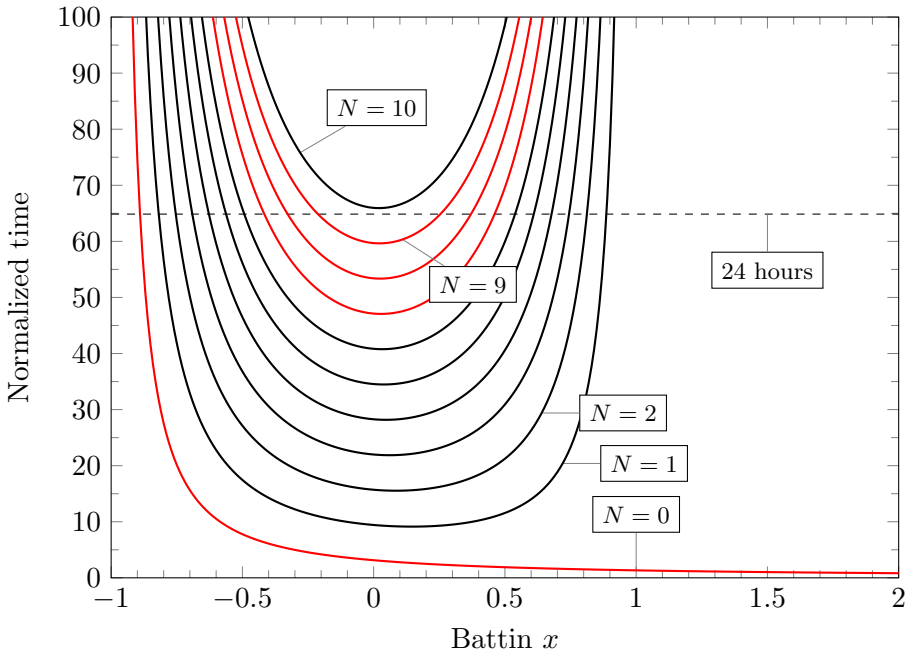

Figure 1: Typical curve of normalized time versus x by whole orbit N; short way only shown

4.3 Solving for orbits

The transformation of variables technique for density calculation requires that *every* Lambert solution be found, the inverse images of the initial value problem, together with the forward Jacobian determinant, be computed. This means each *Lambert mode*: whole orbit count N, all short and long way solutions, and for whole orbit solutions, both left and right of the minimum. For every set of boundary conditions $\boldsymbol{r}_1$, $\boldsymbol{r}_2$ and elapsed time Δt, there is one Lambert mode of each for $N = 0$ and two of each for $N \geq 1$, as can be seen in fig. 1. For each $\boldsymbol{r}_2$ point, the $N = 0$ solutions are first found (at present, unbound orbits are not computed), then the whole orbit minimum times. The maximum N considered is $N_{\max}(\Delta t)$ at any elapsed time; the maximum overall determined from the highest elapsed time desired, $N_{\max}(\Delta t_{\max})$. Then the solution for each of the possible Lambert modes is found.

The normalized time eq. (7) is computed as a function of x, as is its derivative eq. (14). Because the function is not defined for $x \leq -1$, a Newton solver, which is an unconstrained optimization, is not ideal. It is easy to find cases where a guess of a valid x will produce a derivative such that the next iteration of the Newton method gives an invalid value $x \leq -1$. Therefore, we use a hybrid bracketing and Newton solver method. In this approach for the first time step at which there is a solution, the solver moves toward the extreme values of x (depending on the derivative of the function at the current evaluation point), halving the distance to the boundaries $x = \pm 1$ until it has bracketed the desired value. Then, a Newton solver is used to find the exact (within specified tolerance) value of x. There is no problem with Newton convergence here. For subsequent time steps for that location $\boldsymbol{r}_2$, the Newton solver is applied directly to the solution obtained on the previous time step for that Lambert mode. This requires the time steps be small enough that this always converges.

Once the solver has found a value of x that solves eq. (7), the semimajor axis a and change in

eccentric anomaly ΔE may be found. The semimajor axis is computed from a_m using x,

$$a = \frac{a_\mathrm{m}}{1 - x^2} \tag{17}$$

and the change in eccentric anomaly during the elapsed time period

$$\Delta E = 2\pi N + 2\left(\arccos x \pm \arccos y\right), \tag{18}$$

where the sign on the final term is determined by the short $(-)$/long $(+)$ way information. If $x > 1$, the orbit is hyperbolic and the cosines become hyperbolic cosines. The inclusion of the whole orbit count N is important here, as correct (non-normalized) angle is necessary to compute the rest of the orbit. From the determined a and ΔE, the Lagrange coefficients eq. (2) may be rearranged to solve for $\dot{\boldsymbol{r}}_1$,

$$\dot{\boldsymbol{r}}_1 = \frac{\boldsymbol{r}_2 - f\boldsymbol{r}_1}{g}. \tag{19}$$

It is this velocity $\dot{\boldsymbol{r}}_1$ that is needed for the look-up in the velocity distribution function at the fragmentation for the density transformation. Also needed is the Jacobian determinant of the forward map; by calculating $\dot{f}$ and $\dot{g}$, the complete set of inputs to the Jacobian calculation eq. (6) is available.

This procedure determines the mathematical solutions to the Lambert problem. Not all of these are physical solutions, however; any trajectory that intersects the earth will not contribute to the spatial density after the collision. So, earth intersection is determined; if there is no earth intersection, the velocity density G_X is computed for the appropriate distribution, and the spatial density G_Y accumulated into the total for that $\boldsymbol{r}_2$ point. Even when $\Delta t > t_\mathrm{min}$ for a given N, there may be no physical solution, for any of the four mathematical solutions possible. However, as N increases and t_min increases, there may be mathematical and physical solutions possible. In the case plotted in fig. 1, there are 38 mathematical solutions and two physical solutions (one each short and long way) for each of $N = 0$, 7, 8, and 9, and no more, for a total of eight. The corresponding curves are marked in red on the plot; only one each of the whole orbit solutions is a physical solution, so there are four total short way solutions. There are also four long way solutions, ungraphed.

Colinear points $\boldsymbol{r}_1 \parallel \boldsymbol{r}_2$ represent a particular problem for Lambert solvers. Most significantly, an orbital plane is not determined by colinear points, so only the planar elements a, e may be solved. This means that the inverse image of the initial value problem is a continuum of points, so the sum in eq. (1) must be replaced by an integral. We did not perform this calculation; because there are an even number of evenly spaced and symmetrically distributed points in the vertical (perpendicular to the fragmentation) direction, this case is skipped.

5 Initial velocity distribution

The method described has been used to compute the spatial density resulting from the fragmentation of a satellite in a 900 km altitude circular orbit that fragments. From the computation of all physically possible Lambert solutions, the inverse images of each $\boldsymbol{r}_2$, together with the corresponding forward Jacobian determinant, a density is obtained for each point, converted to a color, and rendered in a plot. Simulated are two different initial velocity distributions, G_X, the first being a constant, or "top hat" distribution. The top hat distribution has a value of zero for velocities whose difference from the initial velocity (delta-v) exceeds 2kms^{-1}; for values less than that, it has a constant value equal to the reciprocal volume of a sphere of radius of 2.0. When viewed from delta-v space, it is isotropic. This makes a maximum possible inertial speed of 9.4kms^{-1} which is

less than the escape velocity, so parabolic and hyperbolic orbits are not possible in this particular simulation.

The NASA EVOLVE 4.0 distribution [3] has a value

$$G_X = \frac{1}{2\sqrt{\pi}\sigma^2} \exp\left(-\frac{\left[\log_{10}(\Delta V) - \mu^{\mathrm{EXP}}\right]^2}{2\sigma^2} \right) \tag{20}$$

where the ΔV is the magnitude of the change in velocity in meters/second, and $\sigma = 0.4$. The value μ^{EXP} depends on the area to mass ratio of the fragments. We have chosen to use $\mu^{\mathrm{EXP}} = 1.65$, which corresponds to the EVOLVE model of fragment speed for a fragment area to mass ratio of $0.1\mathrm{m}^2\mathrm{kg}^{-1}$, near the peak of the empirical distribution by area to mass ratio presented in the cited paper. This distribution has a peak at $44.67\mathrm{ms}^{-1}$, and no upper bound. Although the formula has the normalization constant for the normal distribution, it does not integrate to one. The volume integral over all velocity space

$$\int_0^\infty 4\pi v^2 \exp\left(-\frac{\left[\log_{10}(v) - \mu^{\mathrm{EXP}}\right]^2}{2\sigma^2} \right) dv = 0.1176080\mathrm{km}^3 \tag{21}$$

is divided into the spatial densities computed to give a normalized spatial number density. The EVOLVE distribution, like the top hat, is isotropic, so the integrand includes the area of the spherical shell at each value of v.

6 Simulation and results

While the method described allows the computation of density anywhere in space, for presentation purposes and to keep the computation time and data storage required down, only points in the original orbital plane of the simulated satellite were computed. The density map images show this plane from −38256 km from the center of the earth on the left, antipodal to the fragmentation location, to +7800 km on the right where the fragmentation is. In the perpendicular direction, it extends ±12948 km. The asymmetric plot in the horizontal direction was chosen deliberately because most of the interesting density variations are antipodal to the fragmentation location. The mesh points evaluated are every 24 km in both directions, and the evaluation is on a grid of 1920 by 1080 points, corresponding to full high-definition video. Note that for the top hat distribution with a maximum speed of 9.4 km/s at a perigee of 7278 km (900km altitude), apogee radius is 30369 km, and therefore, the left side in this view is unreachable. The EVOLVE distribution, being exponential, has no such upper limit, so there can be positive density almost anywhere on the image plane.

Because Lambert solutions are cylindrically symmetric about the axis of the first point (the fragmentation direction), it is only necessary to solve for half the plane, either the lower or upper half. An initial velocity computed for one half is then reflected about the horizontal axis to determine its value for the mirror location on the other half. Note that the symmetry of the solutions does not necessarily extend to a symmetry of the density: the initial velocity distribution may not be, in fact usually is not, symmetric; an isotropic distribution has equal probability in all directions of the *change* of velocity; once added to the initial velocity of the satellite, it is not symmetric.

The densities obtained from the top hat distribution are either zero, where there is no solution, or in the range of $10^{-14}\mathrm{km}^{-3}$ to $10^{-9}\mathrm{km}^{-3}$ or so. A scale is shown on the plots; the zero density points are plotted as black. The lowest positive densities are plotted in blue, brightening from black to the brightest blue. From $7.5 \times 10^{-13}\mathrm{km}^{-3}$ through $1.0 \times 10^{-10}\mathrm{km}^{-3}$, the hue changes on

a logarithmic scale from blue to magenta to yellow. Densities above $5.0 \times 10^{-10}\text{km}^{-3}$ are shown as white. The densities are normalized number densities, meaning that the number of fragments expected in a volume is the integral of the density of that volume, multiplied by the total number of fragments. There is a small green disk placed on the image representing the "ghost" of the source orbit; in the video sequence[1], one pre-fragmentation orbit is shown in green as well.

The video simulates the ensuing spatial distribution of debris after fragmentation with the top hat distribution, showing the first eight hours at 15 minutes of real time per second of video, and after that, one hour of real time per second, and ends at 36 hours after the fragmentation. Figures 2 to 5 shows several frames from the video. There are many structures apparent from the images. During the very earliest times, Jehn's phase A, which lasts approximately one original orbital period, the cloud forms into a banana shape (including the stem!) that has long been recognized [8]. Then, in phase B, the leading front of the cloud curves around to make a full circle back to the well-known pinch point at about three hours, or two orbital periods. This forms the first of many bands which are well-separated on the antipodal side.

Meanwhile, the outer tail of the lowest density region is moving outward. As time goes on, the leading front keeps cycling, making new bands at the same radius (approximately the radius of the original radius), with the old bands moving outward. After several hours, it is very difficult to see the leading front because it is so narrow.

The "anti-pinch line," or "anti-pinch wedge" as it has been called, is distinctly noticeable after about an hour. It is caused by the appearance of two $N = 0$ (zero orbit) solutions; because the earth blocks long-way solutions that are too close to the original point, the double solution is only possible near the antipodal line. As the first (outer) band moves out of the field of view at about three hours, it takes with it most of that concentrated density. As the new bands form, they each have the concentrated line, but that region of concentration does not persist between bands; it is more a series of line segments.

As new bands are created and move outward, they overlap the old bands, and the boundaries of the bands are clearly visible in this case as superposition of the individual densities. Between the bands, the zero-density gaps on the antipodal side start out very broad, and gradually fill in. At around 18 hours, the bands in the middle are just starting to completely overlap. Notice that the triangular shape gaps are more on the upper half plane than the lower.

Although it is difficult to see at this resolution, the "fronts" of the bands have a sudden drop off in density with increasing radial distance, from the very highest density to actually or almost nothing, while the climb back up in density is much more gradual. Look for the thin magenta line along the outer edge of the band at hours eight through twenty.

The simulation for the NASA EVOLVE distribution with a fixed fragment area to mass ratio of $0.1\text{m}^2\text{kg}^{-1}$ are shown in figs. 6 to 9. Many of the features seen in the top hat distribution are seen here, such as the pinch point, anti-pinch line, and the antipodal bands. That is because these are phenomena of the dynamics rather than the initial velocity distribution. On the other hand, the relative concentration of density nearer the earth, rather than spread out far from the earth, and the lack of sharp cutoff in distance from the earth, are clearly characteristics of the initial Gaussian-logarithm distribution, with peak around 45 m/s, rather than flat distribution with sharp cutoff. More subtly, at around an hour in the EVOLVE sequence, the passing of the antipodal line leaves a high density region there that works its way outward, leaving a fading solid line that is later replaced by the line broken by the bands. This phenomenon, not seen in the top hat distribution, is also clearly distribution dependent.

It bears reminding that this is a two-body simulation only; perturbations will certainly alter the

[1]See `http://www.youtube.com/USNRL`

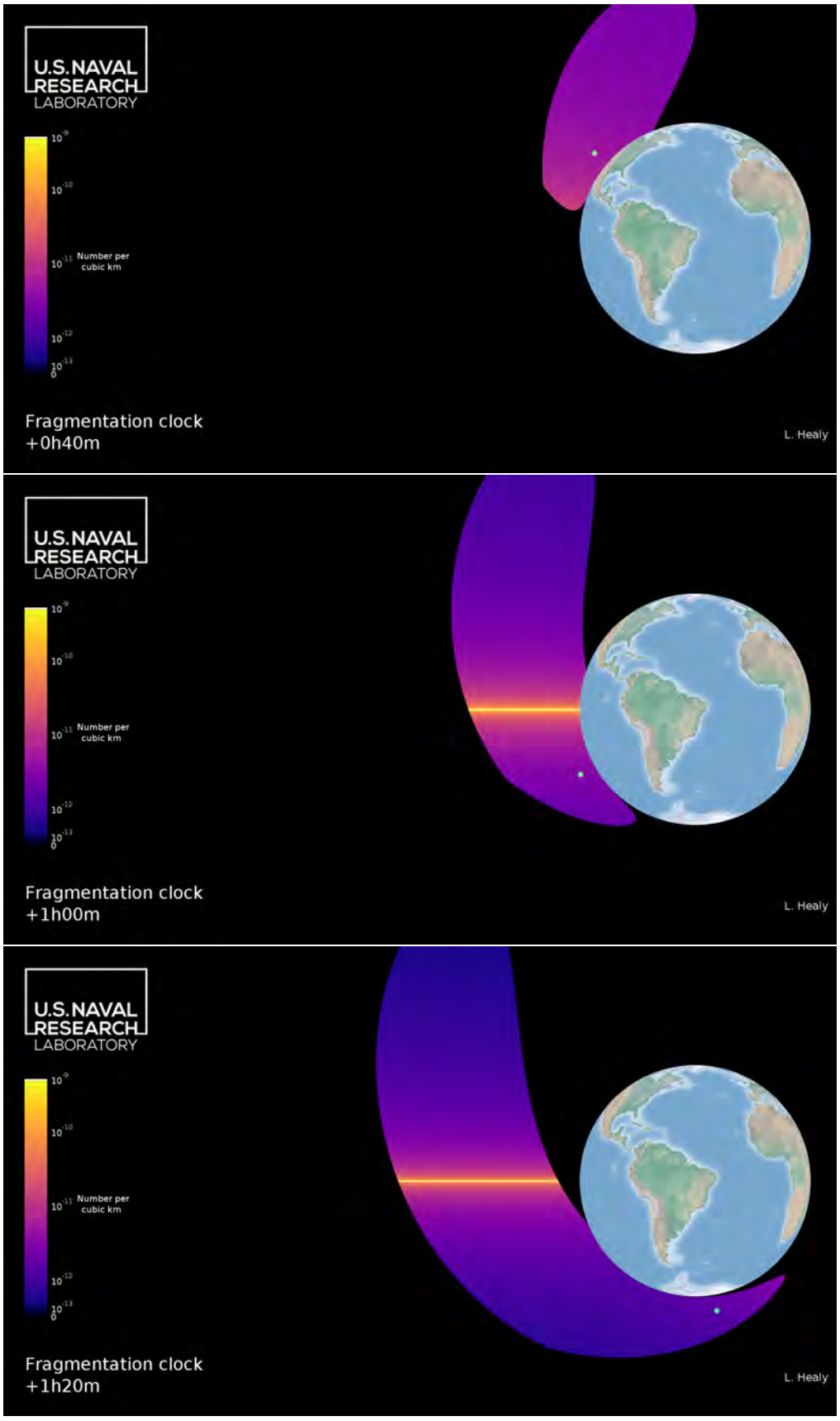

Figure 2: Evolution of spatial density from the top hat 2 km/s velocity distribution

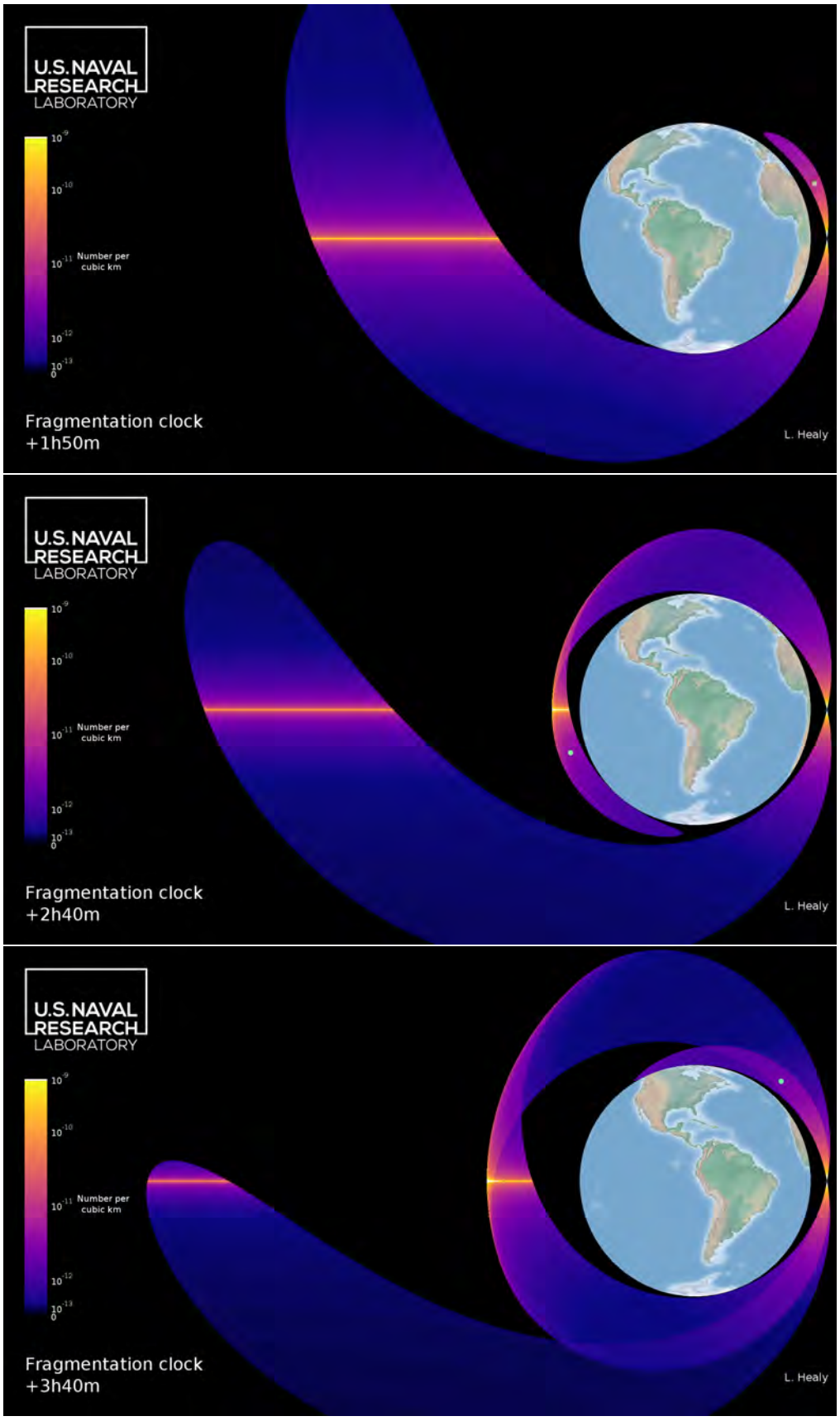

Figure 3: Evolution of spatial density from the top hat 2 km/s velocity distribution

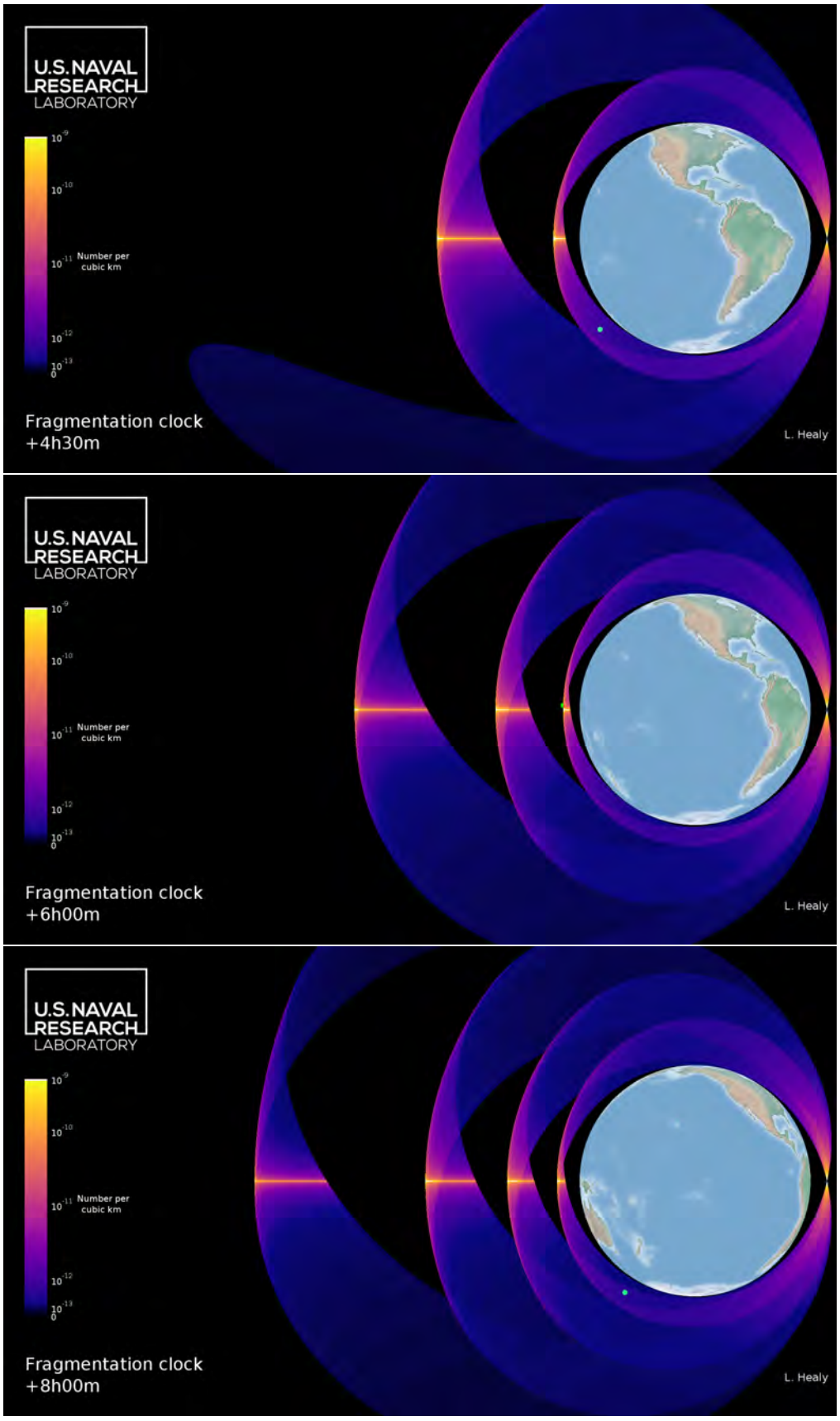

Figure 4: Evolution of spatial density from the top hat 2 km/s velocity distribution

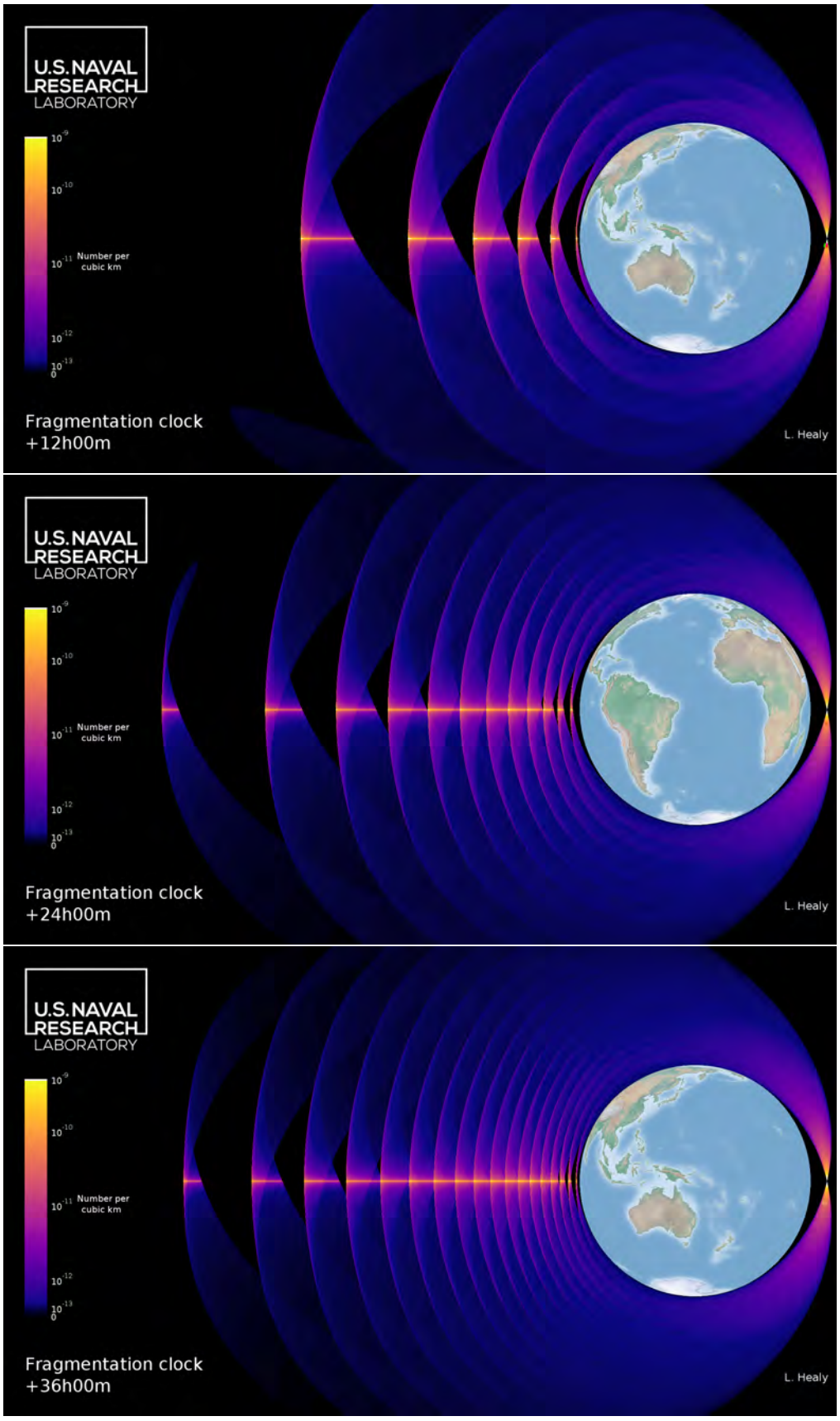

Figure 5: Evolution of spatial density from the top hat 2 km/s velocity distribution

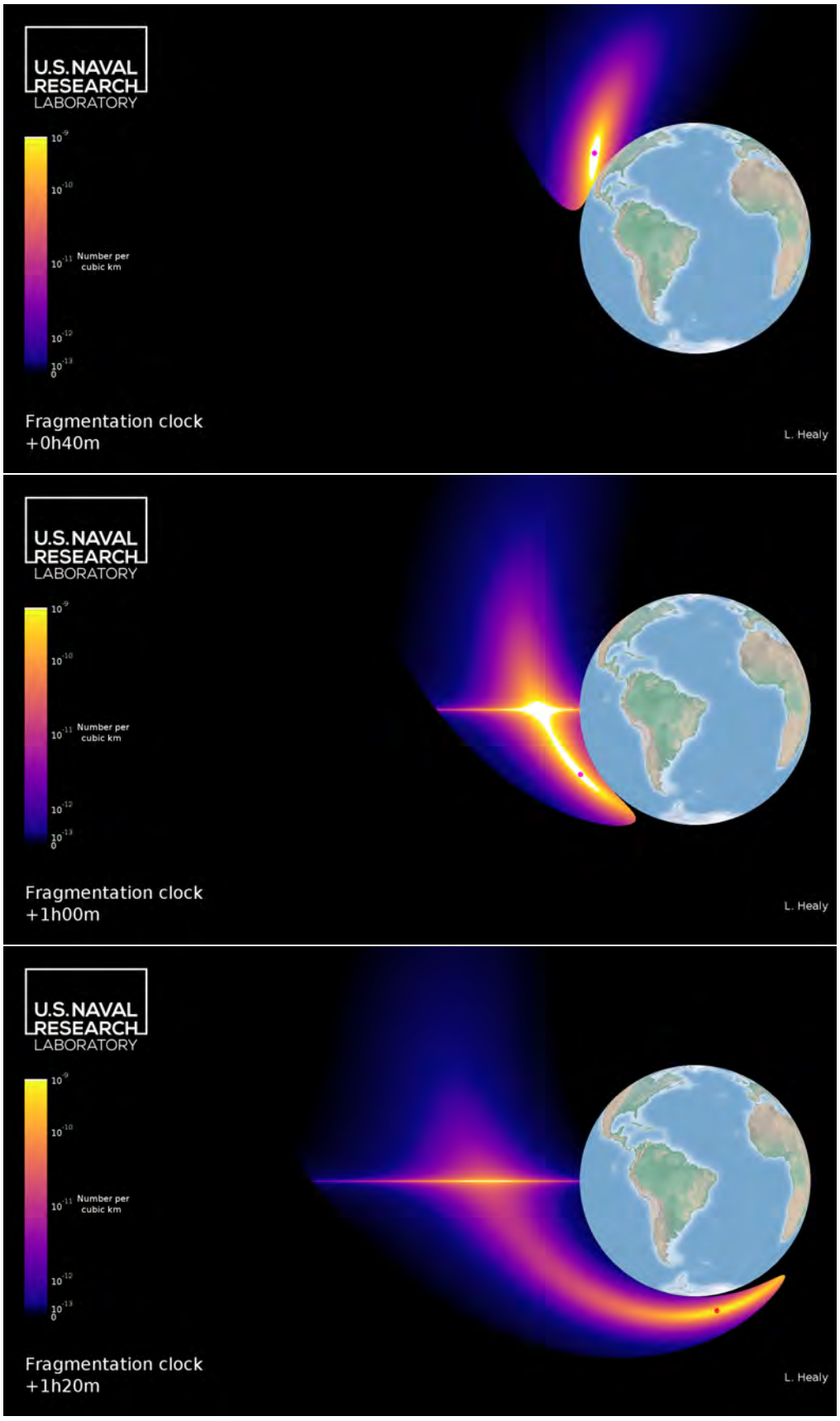

Figure 6: Evolution of spatial density from the NASA EVOLVE 0.1 velocity distribution

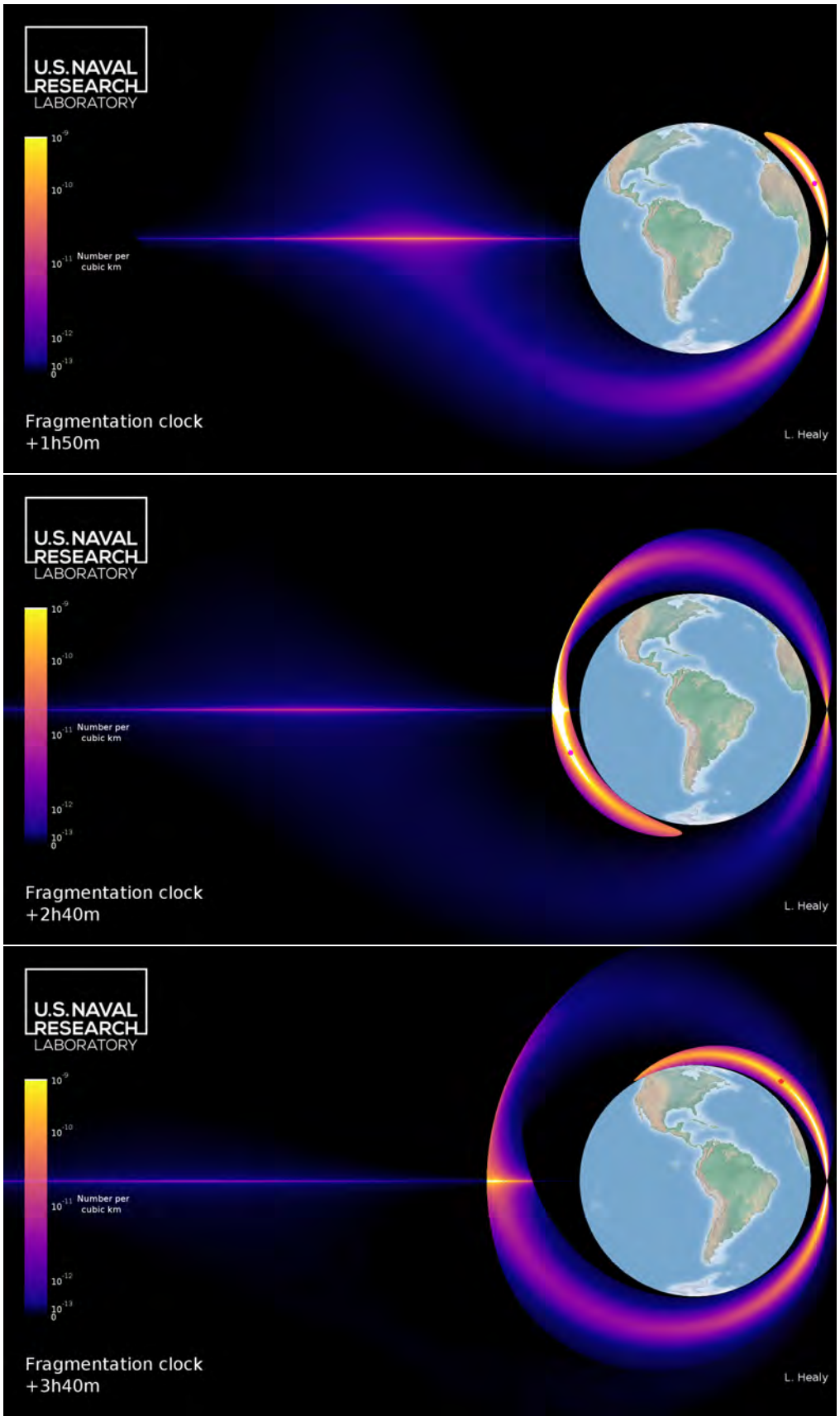

Figure 7: Evolution of spatial density from the NASA EVOLVE 0.1 velocity distribution

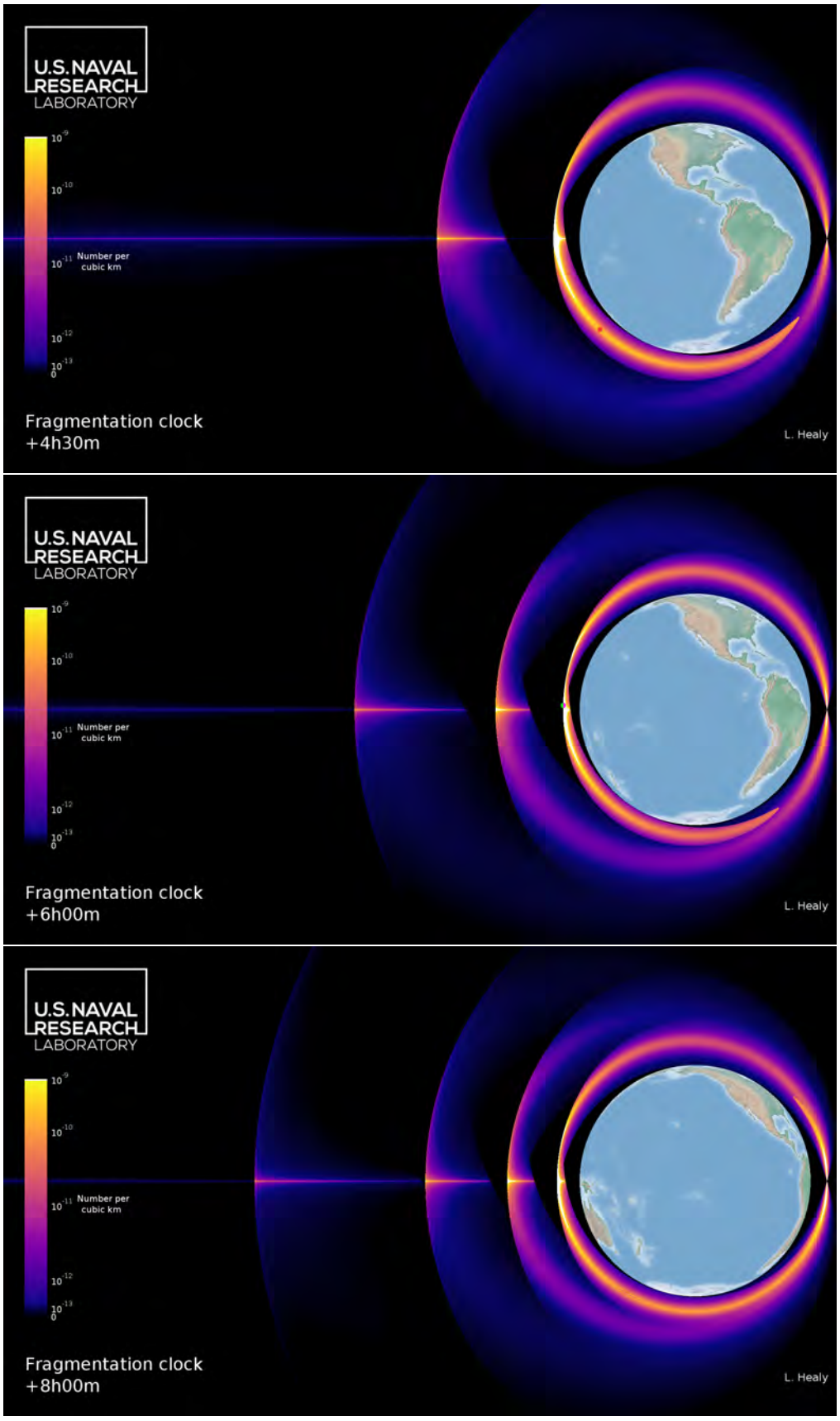

Figure 8: Evolution of spatial density from the NASA EVOLVE 0.1 velocity distribution

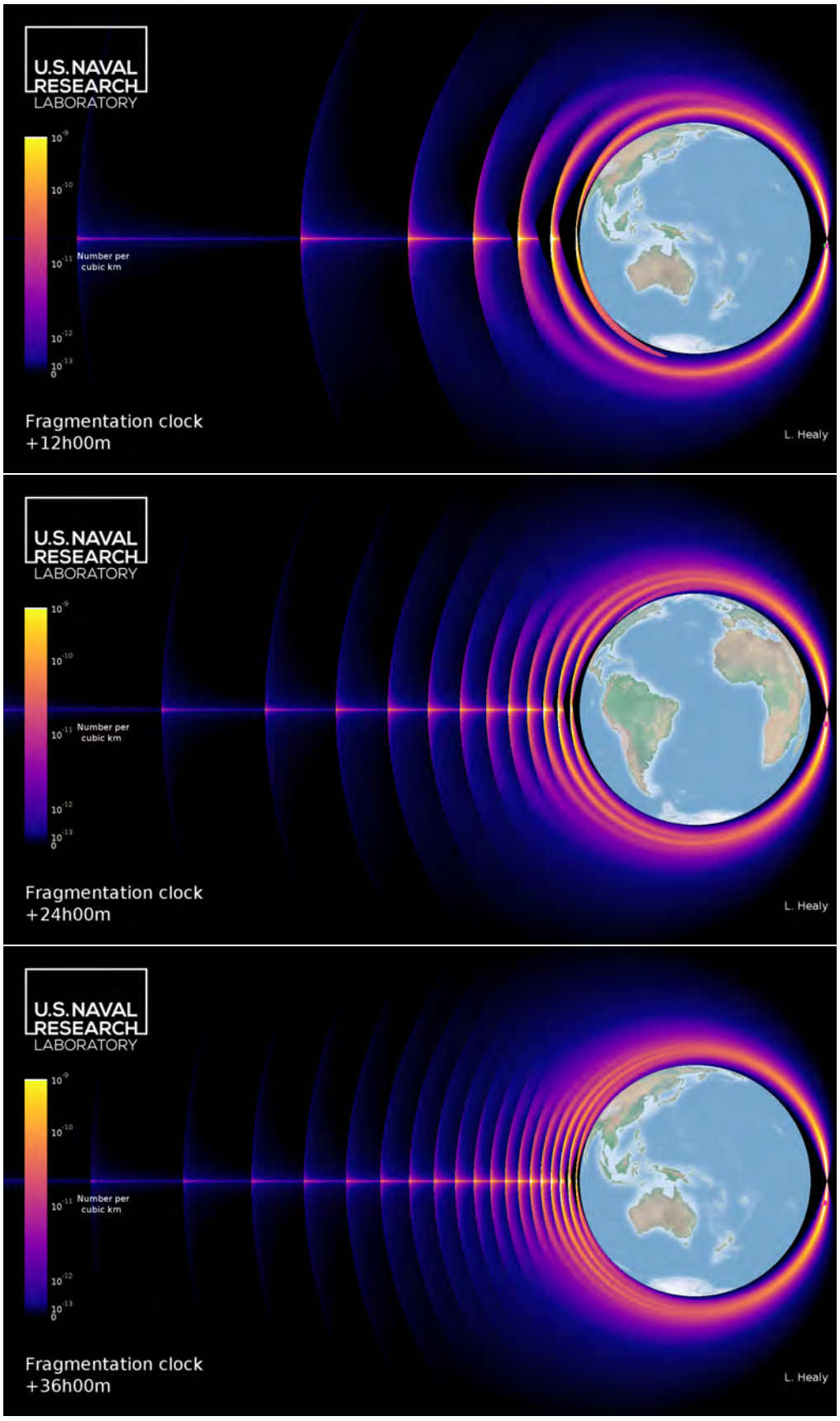

Figure 9: Evolution of spatial density from the NASA EVOLVE 0.1 velocity distribution

appearance, and likely have the effect of smearing together sharp density contrasts, most notably, the bands.

7 Total concentrated volume and its persistence

The volume of space for which density exceeds a given threshold as a function of time is plotted in fig. 10 for thresholds of 10^{-11}km^{-3}, 10^{-10}km^{-3}, and 10^{-9}km^{-3}; the lower plot is an expansion of lower volumes for the latter two threshold values. These figures correspond to the top hat initial velocity distribution. Notice that they seem to settle into steady-state values after a few hours. At density thresholds below about 10^{-11}km^{-3}, there is no settling into a steady-state value.

Figure 11 shows the same plot, but with the NASA EVOLVE 4.0 initial velocity distribution for an area to mass ratio of $0.1\text{m}^2\text{kg}^{-1}$. For this distribution, there is no settling for 10^{-11}km^{-3} within the thirty-six hours simulated. For 10^{-10}km^{-3}, and 10^{-9}km^{-3}, there is settling. An initial transient spike seen is seen at the three thresholds at 72, 60, and 50 minutes, respectively. The original orbital period is 103 minutes, and thus the spike at 10^{-9}km^{-3} occurs when the original orbit crosses the antipodal line. As it approaches the original fragmentation point and forms the pinch point, there is an increase of lower level but concentrated regions of density, and those peaks are a combination of the two phenomena.

To address the question of whether there are fixed inertial locations of high concentrations of debris, we looked at not just places whose density exceeded a threshold, but those places where it exceeded the threshold the previous time step as well. The volume of these persistent high-density regions are plotted in fig. 12 for the top hat distribution and fig. 13 for the NASA EVOLVE 4.0 distribution, and it can be seen that both curves are virtually identical to the corresponding high density volume plots, indicated that almost all the high-concentration locations persist. Again, the lower plot is an expansion of lower volumes (higher threshold). The lowest threshold looks very stable; as is clear from the video, this level masks quite a bit of dynamics as the bands form. At the higher thresholds, the pattern of the total volume and persistent volume look roughly the same, but a close comparison shows that there is a significant unstable concentrated volume until about twenty hours for 10^{-10}km^{-3}, and nine hours for 10^{-9}km^{-3}.

8 Application and further study

Many of those who have studied density propagation have been interested in the uncertain propulsion (or sensing) problem; they usually assume a highly peaked and possible even normal distribution. Unfortunately, as is clear from the forgoing, orbit dynamics in Cartesian coordinates rapidly makes a hash of that assumption!

Although the premise of this study is stated in terms of fragmentation and debris, there is nothing in these results that require the distribution be of actual pieces from a fragmentation. They could as well be a probability distribution, originating from, say, uncertain propulsion. In that case, the isotropic distribution assumed here is not applicable, but the rest of the computation is.

There are many potential improvements and extensions possible. First, the density outside of the original orbit plane in the third dimension would be very interesting; the symmetry of the Lambert solutions makes this computation not too much more time consuming than the two-dimensional computation, but there is a requirement for considerably more data storage.

The effect of perturbations, notably J_2 and drag, would make an interesting alteration to the picture. We anticipate that the inclusion of perturbations will smear some of the sharp changes

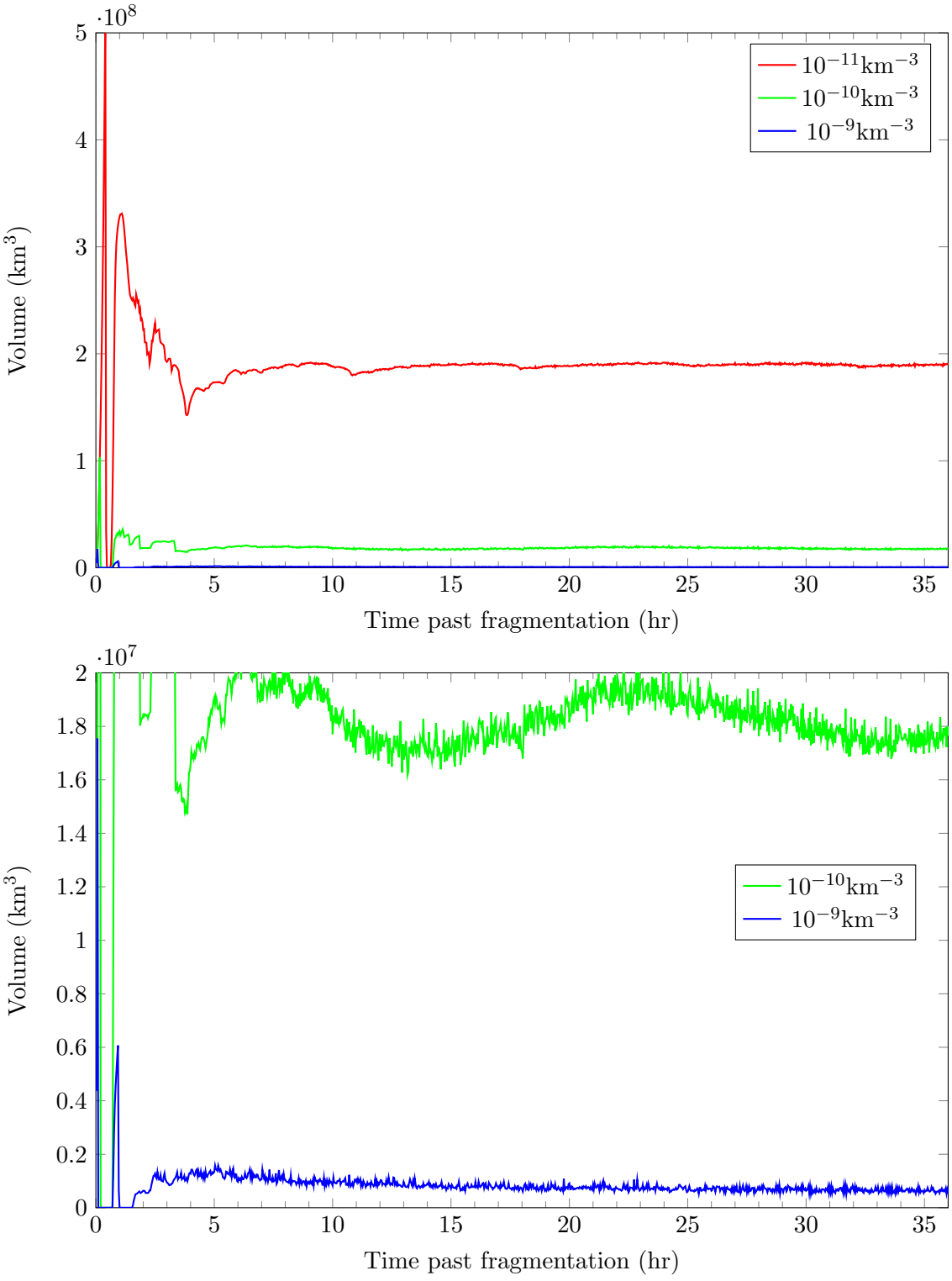

Figure 10: Volume of high density for top hat

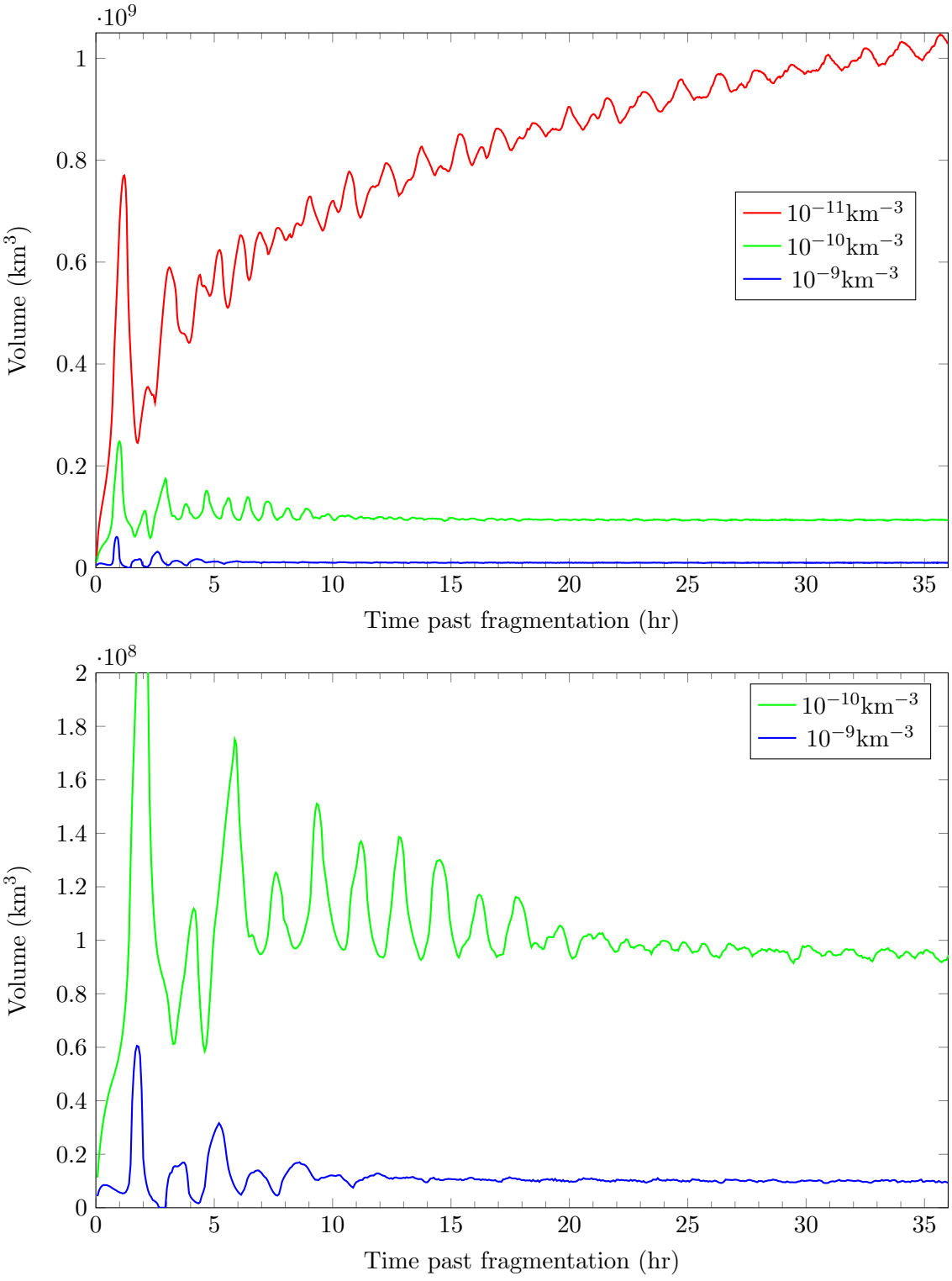

Figure 11: Volume of high density for EVOLVE

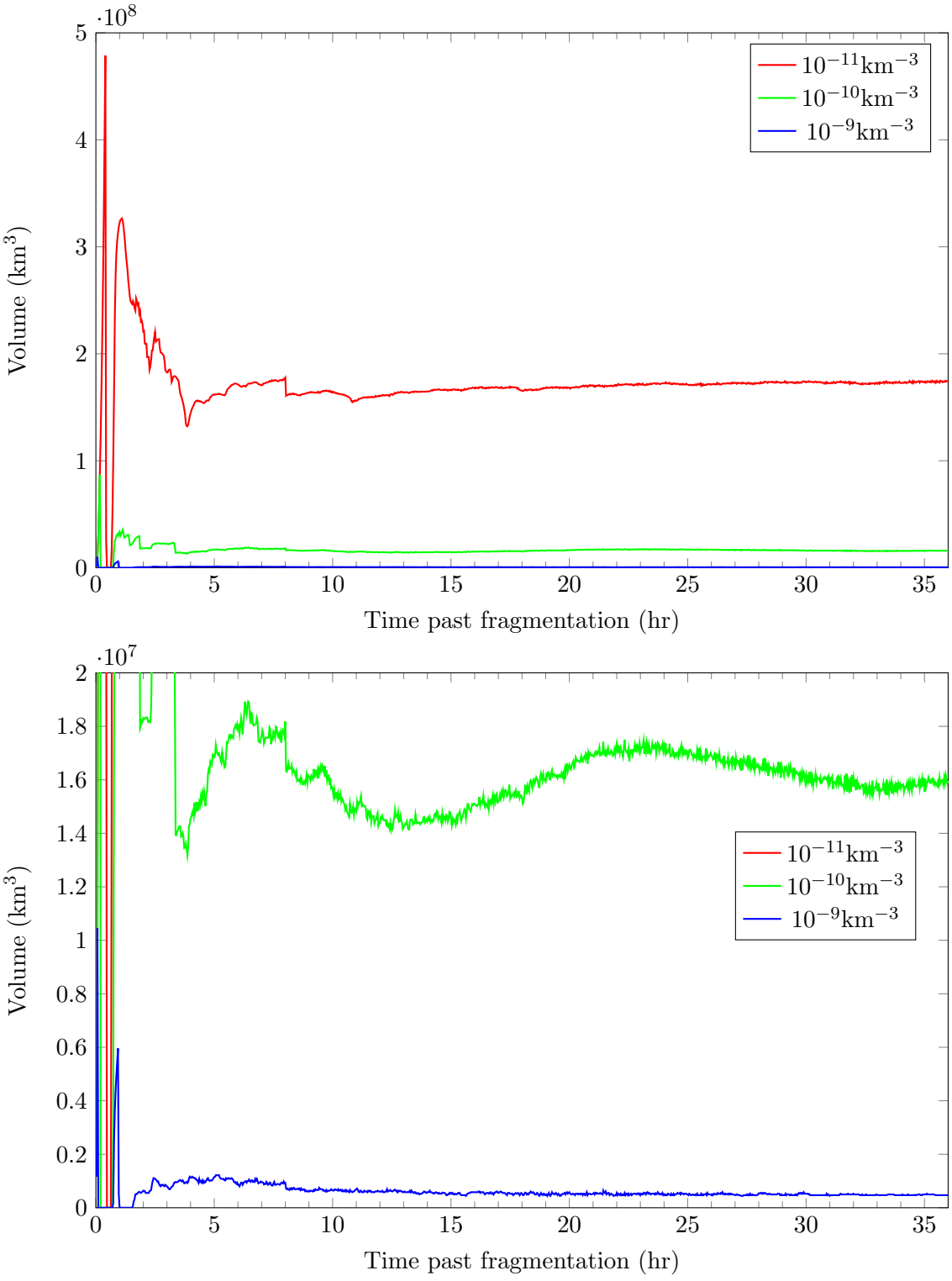

Figure 12: Persistent volume of high density for the top hat distribution

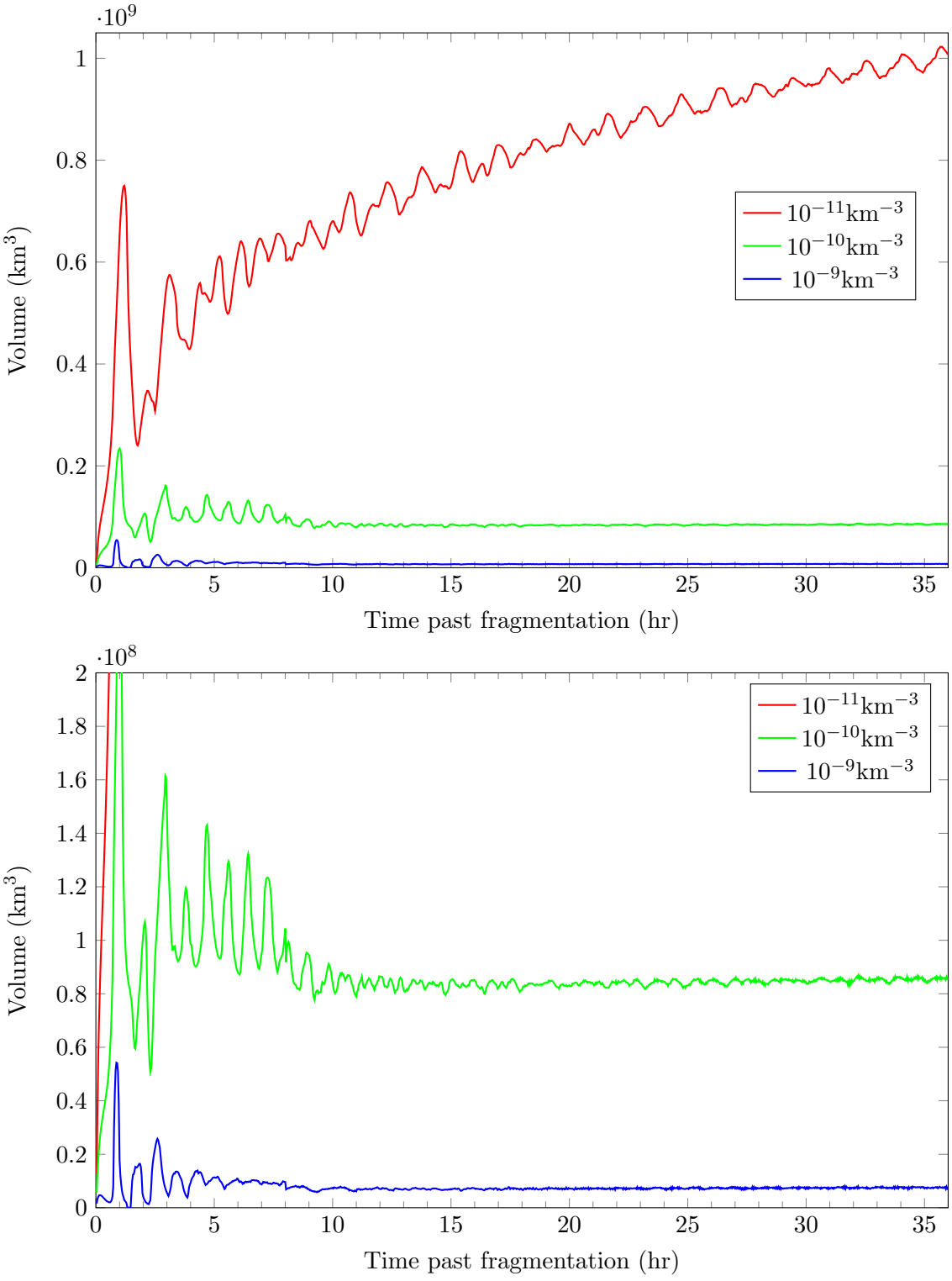

Figure 13: Persistent volume of high density for the EVOLVE distribution

in density and associated structures seen in the figures. In the same way that the earth acts as an occlusion of the orbits, cutting the set of solutions from the mathematical to the physical, the presence of atmospheric drag will effectively expand the radius of the earth from that point of view by removing the lowest orbits, especially for longer elapsed time periods.

9 Conclusion

The near-term aftermath of an orbital fragmentation, on the order of twenty orbits, is quite complicated, consisting not just of the known pinch point and anti-pinch line, but of bands that form on the antipodal side. These bands have the appearance of being generated at the original orbit altitude and move outward. During the later orbits, they spread and merge together, especially toward the earth. Certain features are visible that are dependent on the initial velocity distribution. The NASA EVOLVE 4.0 distribution for fixed area to mass ratio, which has a Gaussian distribution in the logarithm of delta-v, shows a distinct peak in high density a half orbit after the fragmentation, as the original orbit crosses the antipodal line. Though it fades in density, this line persists for few orbits before the bands appear. Common approximations will miss much of these and other notable features.

References

[1] R. Jehn. "Dispersion of debris clouds from In-orbit fragmentation events". In: *ESA Journal* 15.1 (1991), pp. 63–77.

[2] Richard S. Hujsak. "Nonlinear dynamical model of relative motion for the orbiting debrisproblem". In: *Journal of Guidance, Control, and Dynamics* 14.2 (1991), pp. 460–465. ISSN: 0731-5090. DOI: 10.2514/3.20660. URL: http://dx.doi.org/10.2514/3.20660 (visited on 10/05/2015).

[3] N. L. Johnson, P. H. Krisko, J. -C. Liou, and P. D. Anz-Meador. "NASA's new breakup model of evolve 4.0". In: *Advances in Space Research* 28.9 (2001), pp. 1377–1384. ISSN: 0273-1177. DOI: 10.1016/S0273-1177(01)00423-9. URL: http://www.sciencedirect.com/science/article/pii/S0273117701004239 (visited on 10/05/2015).

[4] D. S Sivia and J Skilling. *Data analysis: a Bayesian tutorial.* Oxford; New York: Oxford University Press, 2006. ISBN: 978-0-19-856831-5 978-0-19-856832-2.

[5] David A Vallado and Wayne D McClain. *Fundamentals of astrodynamics and applications.* El Segundo, Calif.; Dordrecht; Boston: Microcosm Press ; Kluwer Academic Publishers, 2001. ISBN: 0-7923-6903-3 1-881883-12-4 978-0-7923-6903-5 978-1-881883-12-8.

[6] Richard H Battin. *An introduction to the mathematics and methods of astrodynamics.* New York, N.Y.: American Institute of Aeronautics and Astronautics, 1987. ISBN: 0-930403-25-8 978-0-930403-25-6.

[7] Nitin Arora, Ryan P. Russell, Nathan Strange, and David Ottesen. "Partial Derivatives of the Solution to the Lambert Boundary Value Problem". In: *Journal of Guidance, Control, and Dynamics* 38.9 (May 29, 2015), pp. 1563–1572. ISSN: 0731-5090. DOI: 10.2514/1.G001030. URL: http://arc.aiaa.org/doi/10.2514/1.G001030 (visited on 12/30/2015).

[8] J. L. Junkins, M. R. Akella, and K. T. Alfriend. "Non-Gaussian Error Propagation in Orbital Mechanics". In: *The Journal of the Astronautical Sciences* 44.4 (1996), pp. 541–564.